Structural and Biological Analysis of the Metal Sites of *Escherichia coli* Hydrogenase Accessory Protein HypB[†]

Alistair V. Dias,[‡] Cory M. Mulvihill,[‡] Michael R. Leach,[‡] Ingrid J. Pickering,[§] Graham N. George,[§] and Deborah B. Zamble*[,‡]

Department of Chemistry, University of Toronto, Toronto, Ontario, Canada M5S 3H6, and Department of Geological Sciences, University of Saskatchewan, Saskatoon, Saskatchewan, Canada S7N 5E2

Received July 15, 2008; Revised Manuscript Received September 1, 2008

ABSTRACT: The [NiFe]-hydrogenase protein produced by many types of bacteria contains a dinuclear metal center that is required for enzymatic activity. Assembly of this metal cluster involves the coordinated activity of a number of helper proteins including the accessory protein, HypB, which is necessary for Ni(II) incorporation into the hydrogenase proteins. The HypB protein from *Escherichia coli* has two metal-binding sites, a high-affinity Ni(II) site that includes ligands from the N-terminal domain and a low-affinity metal site located within the C-terminal GTPase domain. In order to determine the physiological relevance of the two separate sites, hydrogenase production was assessed in strains of *E. coli* expressing wild-type HypB, the isolated GTPase domain, or site-directed mutants of metal-binding residues. These experiments demonstrate that both metal sites of HypB are critical for the maturation of the hydrogenase enzymes in *E. coli.* X-ray absorption spectroscopy of purified proteins was used to examine the detailed coordination spheres of each nickel-loaded site. In addition, because the low-affinity metal site has a stronger preference for Zn(II) than Ni(II), the ligands and geometry for this metal were also resolved. The results from these experiments are discussed in the context of a mechanism for Ni(II) insertion into the hydrogenase protein.

A large number of proteins require transition metal cofactors in order to carry out cellular processes that are integral for survival. Included among this type of proteins are the metalloenzymes carbon monoxide dehydrogenase, acetyl-CoA synthase, urease, and [NiFe]-hydrogenase, all of which contain at least one nickel ion as a catalytic component (*1*). The insertion of the essential metals into the active sites of these enzymes is a strictly controlled process that involves a number of accessory proteins dedicated to the production of a specific enzyme (*1, 2*). These helper proteins must not only deliver the correct metal ions to the enzyme proteins but also ensure that the metal center is assembled in the correct configuration for enzymatic activity. In addition, the complete biosynthesis of many metalloenzymes, including the nickel enzymes listed above, requires GTP hydrolysis that is catalyzed by one of the auxiliary proteins (*3*−*7*).

The *Escherichia coli* hydrogenase enzymes have an active site composed of an intricate nickel- and iron-containing metal cluster required for the reversible production of two protons and two electrons from hydrogen gas (*1, 8*). The assembly of the hydrogenase 3 metal core is dependent on the proteins encoded by at least six genes, *hyp*ABCDEF (*8*−*10*), and HypBDEF are pleiotropic for production of all of the isoenzymes expressed in this organism. Furthermore, the peptidyl-prolyl isomerase SlyD is required for optimal production of the *E. coli* hydrogenases (*11*). The sequence of events is thought to be initiated by the biosynthesis of the iron ligands (carbon monoxide and cyanide) and incorporation of the iron center, followed by insertion of nickel. In the final stage of metallocenter assembly, a specific peptidase cleaves a small C-terminal peptide from the nickel-loaded hydrogenase protein (*8, 10*).

A thorough understanding of hydrogenase biosynthesis may be useful in order to optimize hydrogenase enzyme production for biotechnology and consumable energy applications (*12, 13*), or in evaluating component proteins as antibiotic targets. Our research has focused on nickel delivery, a process carried out by the factors HypA (or the homologue HybF), HypB, and SlyD (*8, 10*). These factors were originally implicated in the nickel insertion step because the hydrogenase deficiency of genetic mutants could be complemented at least partially by supplementation of the growth media with excess nickel. This observation also

[†] This work was supported in part by funding from the Natural Sciences and Engineering Research Council (Canada), the Canadian Institutes of Health Research, and the Canada Research Chairs program. Work at the Stanford Synchrotron Radiation Laboratory is funded by the U.S. Department of Energy and the National Institutes of Health.

* To whom correspondence should be addressed. Phone/Fax: (416) 978-3568. E-mail: dzamble@chem.utoronto.ca.

[‡] University of Toronto.

[§] University of Saskatchewan.

[1] Abbreviations: XAS, X-ray absorption spectroscopy; EXAFS, extended X-ray absorption fine spectroscopy; FT, Fourier transform; EDTA, ethylenediaminetetraacetic acid; G domain, the GTPase domain of HypB consisting of residues 77−290; HEPES, 4-(2-hydroxyethyl)-1-piperazineethanesulfonic acid; IPTG, isopropyl β-D-thiogalactoside; SDS−PAGE, sodium dodecyl sulfate-polyacrylamide gel electrophoresis; TCEP, tris-(2-carboxyethyl)phosphine hydrochloride; Tris, tris-(hydroxymethyl)aminomethane.

10.1021/bi801337x CCC: $40.75
Published on Web 10/23/2008

reveals that these proteins are not critical for other steps in the pathway such as iron complex formation or protein folding.

HypB is a GTPase and mutation of conserved residues that contribute to the enzymatic activity results in decreased nickel incorporation and diminished hydrogenase activity (*3, 14*). The *E. coli* HypB protein also contains two metal-binding sites (*15*). C2, C5, and C7 in the N-terminal CXXCGC motif were identified as ligands of the first site by mutagenesis, and a competition experiment was used to estimate a K_d of approximately 0.1 pM for stoichiometric Ni(II) binding; therefore, this site is referred to as the high-affinity site. This cysteine motif, although common, is not conserved in all HypB homologues (*16*). The existence of the second metal-binding site was evident from a nonlinear increase in the electronic absorption spectrum upon titrating of more than one equivalent of Ni(II) to with the protein. Furthermore, the presence of glycine eliminated the binding of this second nickel while not interfering with the high-affinity nickel. This weaker site was localized to the C-terminal GTPase domain (G-domain[1]) of the protein and mutation of three highly conserved residues within the G-domain of HypB revealed that C166A or H167A selectively disrupted the binding of the second metal, while the C198A mutation weakened it. A G-domain construct (residues 77−290) was used to measure a K_d of 12 μM for Ni(II) and an affinity for Zn(II) approximately 10-fold tighter; hence, this second site is referred to as the low-affinity site (*15*).

Recently, the X-ray crystal structure of a HypB homologue from *Methanocaldococcus jannaschii* (*M. jannaschii*) was solved (*17*). This HypB protein belongs to the class that lacks the N-terminal nickel-binding motif, but the residues identified in *E. coli* HypB as ligands of the low-affinity metal-binding site also serve as metal ligands in the *M. jannaschii* protein. The structure revealed a dinuclear Zn(II) site at a protein dimer interface with two Zn(II) ions bridged by a cysteine residue. One Zn(II) is flanked by two additional cysteine residues from one monomer, while the other is coordinated to a histidine and another cysteine residue from the adjacent monomer, and the remainder of the ligands were refined as water molecules (Figure S4, Supporting Information). Two GTP analogues are also at the dimer interface, and each molecule contacts residues from both monomers.

The detection of the two metal-binding sites on *E. coli* HypB leads to the question of whether either or both are functionally relevant *in vivo* for hydrogenase biosynthesis. Furthermore, characterization of the complete coordination spheres of the two metal sites found in this protein is needed in order to understand the mechanism of action of this protein. By using X-ray absorption spectroscopy (XAS) and *in vivo* microbiology techniques, we have addressed these issues with *E. coli* HypB. Additional analysis was also performed to search for evidence of communication between the two sites.

MATERIALS AND METHODS

Materials. Restriction endonucleases, T4 DNA ligase, and calf intestinal phosphatase (CIP) were purchased from New England Biolabs. *PfuTurbo* DNA polymerase was obtained from Stratagene. Ampicillin, kanamycin, chloramphenicol, TCEP, and IPTG were obtained from BioShop (Toronto, ON). All other reagents were purchased from Sigma except where noted. Primers (Table S1, Supporting Information) were purchased from Sigma Genosys. The Δ*hypB* bacterial strain was prepared from *E. coli DY330* as described previously (*18*). The anti-HypB rabbit polyclonal antibodies were a generous gift from Professor A. Böck (University of Munich, Germany). All metal salts used were a minimum of 99.9% pure (Aldrich) except in the preparation of XAS samples where atomic absorption standard solutions were used (Aldrich). Protein buffer (25 mM HEPES at pH 7.6, adjusted with HCl, and 200 mM NaCl) was treated with Chelex-100 (BioRad) to eliminate trace metal contamination. Water was deionized on a Milli-Q water system to 18.2 megaohms-cm (Millipore).

Plasmids. To prepare the arabinose-inducible vector, the *hypB* coding sequence was amplified by PCR from a pET24b-HypB plasmid (*15*) by using primers HypBforward and HypBreverse (Table S1, Supporting Information). The PCR product was purified by using the QIAquick PCR purification kit (Qiagen) and digested with *Nhe*I and *Xba*I. Following elution from an agarose gel with the QIAquick kit, the fragment was ligated with pBAD24 (American type Culture Collection), digested with the same enzymes, and treated with CIP, and then transformed into XL-2 Blue *E. coli* Ultracompetent cells (Stratagene). The same procedure was used to amplify the HypB GTPase domain (G-domain, residues 77−290) and make pBAD-Gdom except the primers G-domainforward and HypBreverse were used. Plasmid DNA was isolated from cultures grown in ampicillin-supplemented LB media by using the Qiagen HiSpeed Plasmid Miniprep kit. All plasmids were sequenced to verify the constructs (ACGT, Toronto). QuikChange PCR mutagenesis (Stratagene) was used to make point mutants in the pBAD-HypB vector by using the primers listed in Table S1, Supporting Information.

Growth Conditions and Preparation of Crude Cell Extracts. Cells were grown aerobically in LB media overnight prior to 6 h of anaerobic growth in TGYEP adjusted to pH 7.3 and supplemented with 1 μM sodium molybdate, 1 μM sodium selenite, 0.8% glycerol, and 15 mM sodium fumarate as well as arabinose and $NiSO_4$ at the indicated concentrations. Cell extracts were prepared as previously described (*11*) except that the PMSF was replaced with Complete mini, EDTA-free protease inhibitor cocktail (Roche) used at the manufacturer's recommended concentration. The protein concentrations were determined by using the BCA assay (Pierce).

Western Blotting. Crude cell extracts were separated on SDS−PAGE, transferred onto a PVDF membrane, and incubated with a 1:5,000 dilution of the anti-HypB polyclonal antibody, followed by incubation with a goat antirabbit-HRP secondary antibody (BioRad) at a 1:30,000 dilution. Detection was accomplished by using SuperSignal West Pico Chemiluminescence (Pierce), and the bands were quantified by using a Fluorochem 8800 gel documentation system (Alpha Innotech).

Hydrogenase Activity Assays. Crude cell extracts were assayed for total hydrogenase activity by monitoring the hydrogen-dependent reduction of benzyl viologen in solution (*11, 19*). The reactions were prepared in an anaerobic glovebox (95% N_2 and 5% H_2) in a septum-sealed cuvette.

One unit of activity is defined as 1 μmol of benzyl viologen reduced/min with an extinction coefficient of 7,400 M^{-1} cm^{-1}.

XAS Sample Preparation. Both full-length HypB and the G-domain protein, which lacks the N-terminal region and the high-affinity nickel-binding activity, were prepared as described (*15*). For the XAS samples, the protein solutions were concentrated by using an Amicon Ultra Centrifugal Filter Device (Millipore, MWCO = 5000 Da) to an approximate volume of 200 μL. Ni(II) binding produces a shoulder at 320 nm and results in an increased absorbance at 280 nm (*15*); therefore, the concentrations of nickel and protein were calculated on the basis of extinction coefficients at both 280 and 320 nm for Ni(II)-bound HypB. We have previously demonstrated that one equivalent of nickel quantitatively fills the high-affinity site of HypB and that one equivalent of zinc can displace nickel from the low-affinity site but not the high-affinity site (*15*). The concentration of the full-length HypB sample was 1 mM, and after measuring the amount of Ni(II) already bound, an appropriate amount of Ni(II) was added to ensure that the high-affinity site or both sites were filled (1 or 2 equivalents). For Zn(II) XAS, the low-affinity site of full-length HypB (1.4 mM) was filled with 0.7 equivalents of Zn(II), while the high-affinity site was fully loaded with Ni(II). The concentration of the Ni(II)-G-domain was calculated to be 1.8 mM and filled with 0.8 equivalents of Ni(II), while the Zn(II)-loaded protein concentration was slightly higher at 2.2 mM and filled with 0.5 equivalents of Zn(II). For all samples, the metal was added on ice to suppress protein aggregation. Glycerol and TCEP were then added to final concentrations of 20% (v/v) and 1 mM, respectively. The protein concentrations were later confirmed by incubating a small aliquot with 10 mM EDTA and 5 mM TCEP in an anaerobic glovebox over 4 days at 4 °C and using the extinction coefficient at 280 nm of 16 500 M^{-1} cm^{-1} for HypB and 14 355 M^{-1} cm^{-1} for the G-domain (*15*), and the metal content was confirmed by PAR-HPLC metal analysis (*20*). The samples were subsequently frozen with liquid nitrogen and stored at −80 °C before being thawed, transferred to (2 × 10 × 10 mm) Lucite sample cuvettes, and frozen again in liquid nitrogen for data acquisition.

X-ray Absorption Spectroscopy. XAS measurements were carried out at the Stanford Synchrotron Radiation Laboratory (SSRL) with the SPEAR 3 storage ring containing between 85 and 100 mA at 3.0 GeV. For both nickel and zinc data, the K-edge data were collected on the structural molecular biology beamline 9−3 that was operated with a wiggler field of 2 T and employed a Si(220) double-crystal monochromator. The beamline was also equipped with a rhodium-coated vertical collimating mirror upstream of the monochromator and a downstream bent-cylindrical focusing mirror, also rhodium coated. Harmonic rejection was accomplished by setting the angle of the mirrors to a 13 keV cutoff. Incident and transmitted X-ray intensities were monitored using nitrogen-filled ionization chambers, and X-ray absorption was measured as the Ni(II) or Zn(II) Kα fluorescence excitation spectrum using a 30-element germanium detector (*21*). Samples were maintained at a temperature of approximately 10 K by using an Oxford instruments liquid helium flow cryostat. For each sample, 4−19 scans were collected, and the energy was calibrated by reference to the absorption of a nickel or zinc metal foil measured simultaneously with each scan, assuming a lowest-energy inflection point of 8331.6 and 9665 eV for Ni(II) and Zn(II), respectively.

Table 1: Best Ni(II) EXAFS Curve-Fitting Results for the High-Affinity and Low-Affinity Metal Sites in *E. coli* HypB[a,b] (See Table S2, Supporting Information for Additional Fits)

	A-Bs	N	R (Å)	σ^2 (Å^2)	ΔE_0 (eV)	F-factor
			Ni(II)-HypB			
fit 1	*Ni−S*	*3*	*2.168(7)*	*0.00357(1)*	*−17.954(2)*	*0.198*
	Ni−N	*1*	*1.867(34)*	*0.00693(4)*		
fit 2	Ni−S	3	2.174(5)	0.00476(4)	−13.5[c]	0.216
	Ni−N	1	2.065(26)	0.00200[c]		
			Ni(II)-G-domain			
fit 3[d]	*Ni−S*	*1*	*2.166(6)*	*0.00802(16)*	*−13.6(4)*	*0.171*
	Ni−N	*5 (1 Im)*	*2.067(4)*	*0.00448(1)*		
fit 4	Ni−N	6	2.063(2)	0.00482(1)	−11.1(3)	0.209
			Ni(II)/Zn(II)-HypB			
fit 5	*Ni−S*	*3*	*2.148(18)*	*0.00704(1)*	*−17.77(3)*	*0.253*
	Ni−N	*1*	*2.021(12)*	*0.00326(1)*		
fit 6	Ni−S	2	2.171(12)	0.00611(1)	−12.683(2)	0.242
	Ni−N	2	2.022(17)	0.00475(1)		

[a] A-Bs denotes absorber and backscatterer interaction; N denotes coordination number; R is given in Å and represents interatomic distances; σ^2 given in Å^2, are the Debye−Waller factors (mean-square deviations in interatomic distance); the threshold energy shifts, ΔE_0 are given in eV. The values in parentheses are the estimated standard deviations obtained from the diagonal elements of the covariance matrix. The F-factor or fit-error function is defined as $(\Sigma k^6(\chi(k)_{calcd} - \chi(k)_{exptl})^2/\Sigma k^6\chi(k)_{exptl}^2)^{1/2}$. The summation is over all data points included in the refinement. [b] The best fit models are italicized and overlaid in Figure 4. [c] The values for these parameters were fixed on the basis of fits for known square-planar Ni(II) complexes. [d] The fit includes one Ni-Im(N) pathway within the first shell of five nitrogens at a distance of 2.067 Å. This was calculated and inserted on the basis of methods previously described (see ref *38*).

XAS Data Analysis. XAS data reduction was performed with the EXAFSPAK suite of computer programs (http://ssrl.slac.stanford.edu/exafspak.html), employing a Gaussian pre-edge function, and a weighted polynomial spline with normalization correction to extract the EXAFS oscillations, $\chi(k)$. The EXAFS was quantitatively analyzed by curve-fitting $\chi(k)$ directly (as opposed to analysis of Fourier transformed data) as described by George et al. (*22*), using ab initio theoretical phase and amplitude functions calculated using FEFF, version 7.2 (*23*). Phase-shifted Fourier transforms were calculated using theoretical phase functions from the largest EXAFS component. Donors that could be fit as nitrogen or oxygen were fit as nitrogen unless histidines or oxygen donors were the only appropriate ligands based on analysis of the protein sequence within a given metal site. To fit EXAFS arising from histidine ligands coordinated to Ni(II) or Zn(II), the following method was devised (fit 3, Table 1 excluded). Using FEFF 8.25 (*23*), theoretical phase and amplitude parameters for both single and multiple scattering pathways containing second and third coordination sphere imidazole C and N atoms were abstracted from the EXAFSPAK program Mol-Opt. This program created 23 possible scattering pathways, and all were including during fitting analysis; however, for clarity only the direct Ni−imidazole (Ni−N_{im}) or Zn−imidazole (Zn−N_{im}) scattering pathways are shown in Tables 1 or 2 (also applies to Table S3, Supporting Information). No smoothing, filtering or related operations were performed on any of the data.

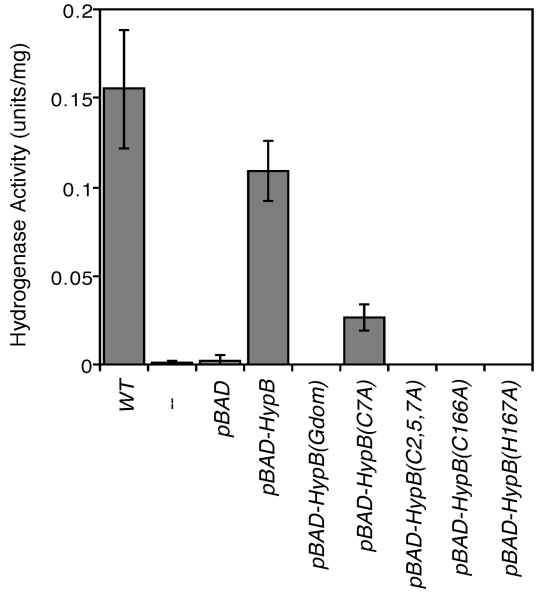

FIGURE 1: Hydrogenase activity produced by HypB mutants. The wild-type *DY330* (WT) or Δ*hypB* cells transformed with the indicated pBAD vectors were grown anaerobically in TGYEP containing fumarate, glycerol, 1 μM nickel, and either 25 μM (WT, Δ*hypB*, pBAD, pBAD-HypB) or 50 μM arabinose. Cell extracts were prepared and tested for hydrogenase activity with the anaerobic benzyl viologen solution assay. The results represent the average of at least three experiments, and the error bars indicate ± SD.

RESULTS

Complementation of a ΔhypB Strain with Inducible pBAD-HypB. To assess the role of HypB *in vivo*, *hypB* was expressed from an inducible pBAD24 vector transformed into a Δ*hypB* strain of *E. coli*. The cells were grown in media supplemented with glycerol and fumarate rather than glucose and formate because the P_{BAD} promoter is repressed by glucose (*24*). These conditions promote the expression of hydrogenases 1 and 2, although hydrogenase 3 is still expressed at low levels (*25*). Western blot analysis confirmed that expression of HypB from pBAD-HypB can be completely repressed by glucose and that upon titration with arabinose there is an increase of HypB expression, with near-wild-type levels of expression obtained when cells are grown in media containing 25 μM arabinose (data not shown).

To measure the hydrogenase activity, cell lysates were added to a solution of benzyl viologen prepared in a hydrogen-containing atmosphere, and the reduction of benzyl viologen was monitored at 600 nm (*11, 19*). As previously demonstrated (*14, 26, 27*), HypB is necessary for the production of active hydrogenase (Figure 1). Cell extracts of the Δ*hypB* strain produced background levels of hydrogenase activity (0.001 ± 0.001 units/mg) as did the same strain transformed with empty pBAD vector as a control (0.002 ± 0.003 units/mg). The hydrogenase activity was restored almost to wild-type levels when *hypB* was induced from the pBAD-HypB vector (0.11 ± 0.02 units/mg) (Figure 1), demonstrating that the protein is functional when it is expressed from this vector.

Hydrogenase Activity is Deficient upon Expression of the HypB Metal-Binding Site Mutants. The physiological relevance of each of the two metal-binding sites of HypB was investigated by measuring the hydrogenase activity of Δ*hypB* cells transformed with the *hypB* gene containing mutations of the appropriate metal-binding residues. First, cells transformed with a vector that only expressed the HypB G-domain, which lacks the first 76 amino acids of HypB and the high-affinity nickel site, produced no detectable hydrogenase activity (Figure 1). To determine if this result was due to the removal of some section of the N-terminal sequence other than the high-affinity metal-binding site, point mutations were made to the cysteines in the N-terminal CXXCGC motif, which are ligands of this site. The hydrogenase activity of cells expressing a C7A mutant was reduced to about 15%, while the triple mutant C2,5,7A was not active (Figure 1). This result correlates with *in vitro* metal-binding experiments that revealed that mutation of a single cysteine in the CXXCGC sequence weakens the high-affinity nickel-binding activity of HypB and that the triple mutation completely abrogates it (*15*).

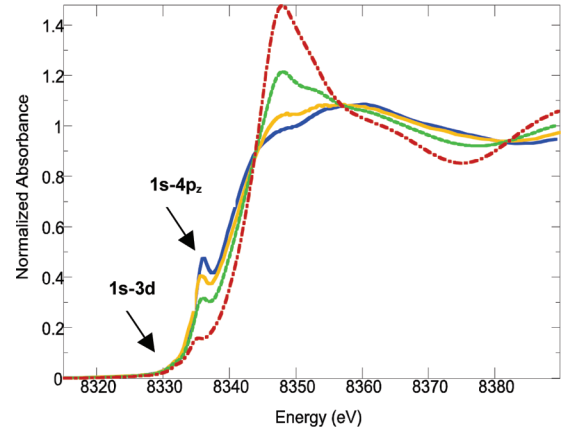

FIGURE 2: Ni(II) near-edge spectra. The overlaid spectra have been normalized to the edge jump. The samples include HypB loaded with 1 equivalent of Ni(II) (Ni(II)-HypB, blue line), HypB loaded with 1 equivalent of Ni(II) in the high-affinity site and 0.7 equivalents of Zn(II) in the low-affinity site (Ni(II)/Zn(II)-HypB, orange line), HypB loaded with 2 equivalents of Ni(II) (Ni(II)/Ni(II)-HypB, dashed green line), and the G-domain loaded with 0.8 equivalents of Ni(II) (red dot-dash-dot line). The arrows indicate the 1s-3d and 1s-4p_z transitions.

Point mutations were also introduced at two of the metal-binding residues in the low-affinity site, C166A or H167A, and neither mutant produced detectable hydrogenase activity (Figure 1). Western blots were used to confirm that upon induction with arabinose, the expression of full-length HypB or the mutants was at least as high as that detected in the wild-type extracts (data not shown), in contrast to a previously mentioned system (*8*). These results clearly demonstrate that both of the metal-binding sites are necessary for the role of HypB in the bioactivation of hydrogenase *in vivo*. Furthermore, the hydrogenase activity in the strains expressing the mutant proteins was partially restored upon the addition of 1 mM nickel to the growth media (10−25%, data not shown), as previously observed for the Δ*hypB* lesion (*3*).

Ni(II) Near-Edge Spectra Analysis. The Ni−K edge spectra of full-length Ni(II)-HypB (loaded with one equivalent of nickel in the high-affinity site), Ni(II)/Zn(II)-HypB (loaded with Ni(II) in the high-affinity site and Zn(II) in the low-affinity site), and the isolated G-domain (with Ni(II) in the low-affinity site only) are compared in Figure 2. The absorption edges range between 8339−8342 eV, which is typical for Ni(II) complexes (*28*). The different features of

the edges for the high- and low-affinity sites are quite evident. The slightly lower edge energy (8339 eV) and the rounded shape of the curve for the Ni(II)-HypB sample is reflective of a square-planar site with high sulfur content (*28, 29*). A small pre-edge feature with very low intensity at 8332 eV is indicative of a 1s-3d transition, and for centrosymmetric sites (i.e., square planar), this peak is normally absent or very weak. The most prominent pre-edge feature centered around 8335 eV can be assigned to a 1s-4p_z electronic transition with shakedown contributions and is diagnostic of four coordinate, planar Ni(II) complexes (*28, 29*) (see Figure S1, Supporting Information, for a comparison of edge spectra from Ni(II) model complexes of known geometry).

A comparison of the Ni(II) spectra of Ni(II)-HypB and Ni(II)/Zn(II)-HypB reveals small but reproducible differences (Figure 2). Upon addition of zinc to the low-affinity site, the edge for Ni(II) in the high-affinity site is still typical of a square-planar geometry; however, Ni(II)/Zn(II)-HypB displays a slightly less intense 1s-4p_z transition at 8335 eV and a slightly more intense edge peak at 8342 eV. These changes in the nickel edge may point toward a reduction in sulfur content or possibly a modest distortion in the square-planar configuration compared to that of Ni(II)-HypB without zinc (*28, 30*).

The spectrum of the G-domain loaded with Ni(II) in the low-affinity site has a steep rising edge well above the highest intensity peak of the full-length HypB sample, and the overall shape of the curve reflects an octahedral site. The sharpness and the position of the edge (8341 eV) is also indicative of a site with significant (N/O) content (*28, 31*). For octahedral complexes, the 1s-3d pre-edge peak is again fairly weak; however, it is usually stronger in intensity for six-coordinate geometries than four-coordinate complexes because of increased p-d mixing (*28*). The intensity of the 1s-3d peak for the Ni(II)-loaded G-domain located at 8332 eV is somewhat lower than expected, and a small pre-edge peak corresponding to the 1s-4p_z transition was also observed at 8335 eV. Penta-coordinate square pyramidal Ni(II) sites exhibit distinctive shoulder-like features before the main edge peak in this region (*28, 29*), but the position and sharpness of the peak in addition to the lower than expected intensity of the 1s-3d peak are more indicative of a mixture containing mainly an octahedral complex and an extremely small population with tetragonal geometry. Comparing the peak intensity of typical tetragonal species (e.g., that of the high-affinity nickel) suggests that this species, if present, corresponds to 10% or less of the total Ni(II). The sample in which full-length HypB was loaded with two equivalents of Ni(II) (in both the high- and low-affinity sites) provides an average spectrum of the separate sites, with features indicative of both six-coordinate and four-coordinate geometries. Subtraction of the Ni(II)-loaded low-affinity site (Ni(II)-Gdomain) spectrum from this sample produced a curve similar to that of the high-affinity site alone (Ni(II)-HypB) and vice versa (data not shown).

Zn(II) Near-Edge Spectra Analysis. The near-edge spectra for two samples with Zn(II) loaded in the low-affinity site of HypB, either in the isolated G-domain or in the context of the full-length protein with Ni(II) occupying the high-affinity site (Ni(II)/Zn(II)-HypB) are shown in Figure 3. Zn(II) has full d-orbitals, and therefore, there is a noticeable absence of any characteristic pre-edge features that could provide information regarding the coordination environment (*32*). However, a shift in the first peak to higher edge energies can generally be associated with an increase in the number of ligating atoms (*32*). The position of the first peak for both HypB and the G-domain are similar (E_o = 9663.7 eV), which indicates that the metals have similar geometries in the two constructs, possibly 4-coordinate and tetrahedral, which is most common for Zn(II), as higher edge energies usually reflect 5- or 6-coordination environments. Furthermore, an examination of Zn(II) model complexes revealed that the relative intensities of the two near-edge spectra peaks are a reflection of the composition of the ligand sphere (*33*). A ligand shell consisting of more light atoms, such as O or N, tends to produce a more intense second peak, whereas it is relatively weaker in a complex composed exclusively of sulfur. On the basis of this analysis, the near-edge spectra of both proteins suggests a mixed $S_x(O/N)_x$ set of ligands with a slightly higher sulfur content apparent in the G-domain site.

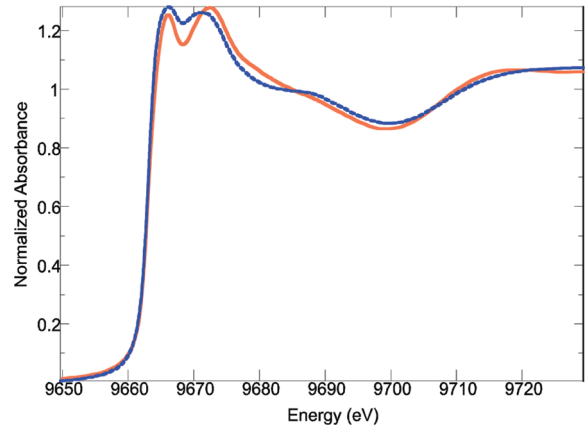

FIGURE 3: Zn(II) near-edge spectra. The overlaid spectra have been normalized to the edge jump. The spectra are for HypB loaded with 1 equivalent of Ni(II) and 0.8 equivalents of Zn(II) (Ni(II)/Zn(II)-HypB, red line) and the G-domain loaded with 0.5 equivalents of Zn(II) (blue dashed line).

Ni(II) and Zn(II) EXAFS Fitting Analysis. Figures 4 and 5 display the raw EXAFS data and best fits as well as the Fourier transforms (FT's) for the Ni(II) and Zn(II) spectra, respectively. The best model fits are italicized and listed in Tables 1 and 2 (as well as fits 2, 4, and 6, Table 1; and fits 2, 4, and 5, Table 2; see below), and additional model fits are listed for comparison purposes in Supporting Information.

The EXAFS FT of HypB loaded with 1 equivalent of Ni(II) (Figure 4B) displays minor and major features at approximately 1.87 and 2.17 Å (fit 1, Table 1), and is best fit to 1 (N/O) donor and 3 sulfurs at those distances, respectively, which are commonly observed in 4-coordinate square-planar environments (*30, 34*). Fit 2 (Table 1) is also a fit of these data to 3 sulfurs and 1 (N/O) donor, but in this case the Debye−Waller factor and the ΔE_o parameters were fixed to values calculated from EXAFS fits for several small molecule square-planar Ni(II) complexes. However, although these values may be more common, the *F*-factor increased, indicating a worse fit. Furthermore, the Ni-(N/O) distance lengthened significantly from 1.87 Å to 2.07 Å, a distance that differs from typical Ni-(N/O) distances in square-planar complexes (*30, 34*). On the basis of this information, it was concluded that the fixed parameters in fit 2 (Table 1), although reasonable, could not be used to properly fit our

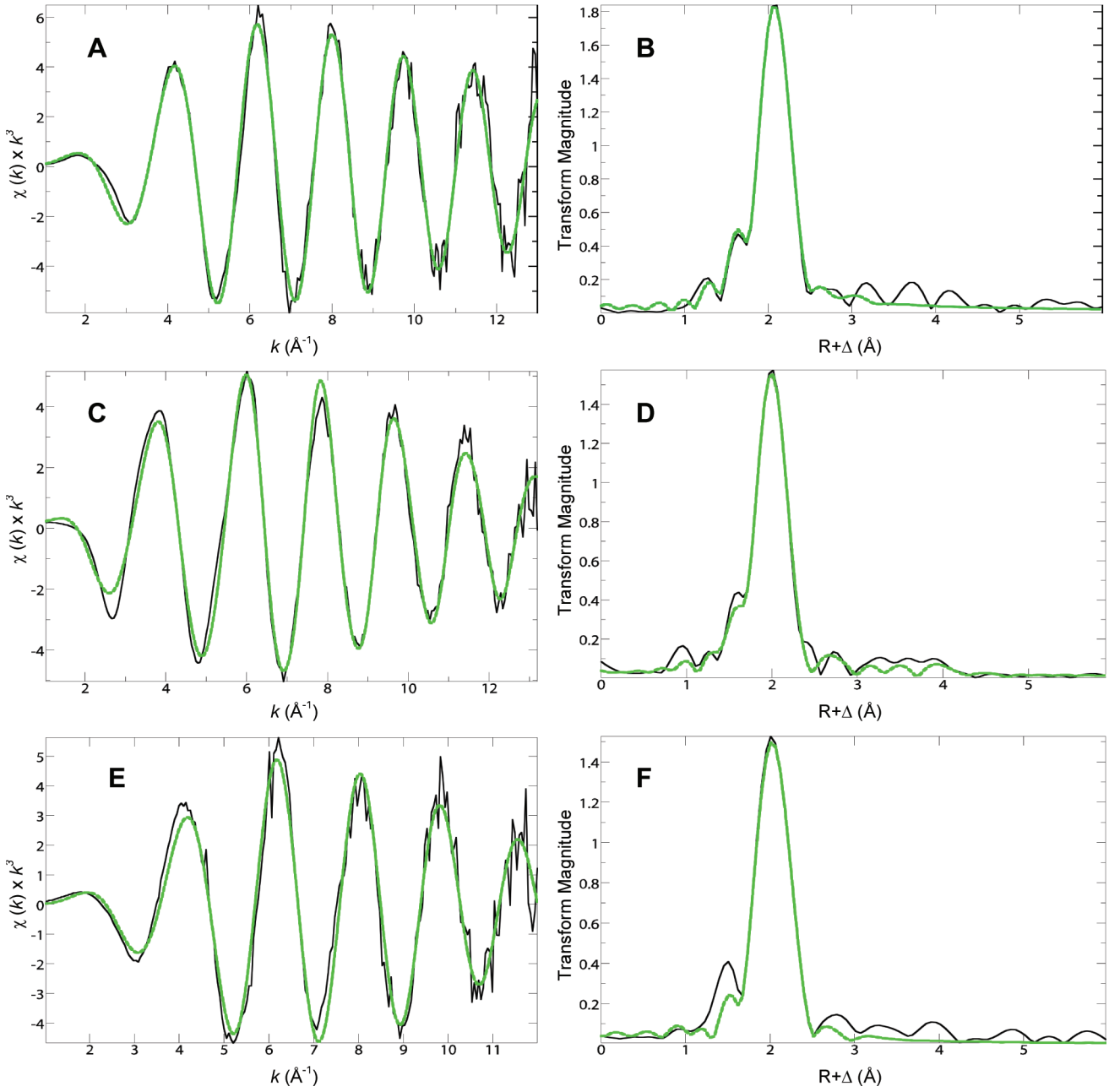

FIGURE 4: k^3-Weighted Ni(II) EXAFS data (left) and Fourier Transform data (right). (A and B) HypB loaded with 1 equivalent of Ni(II). (C and D) G-domain loaded with 0.8 equivalents of Ni(II). (E and F) HypB loaded with 1 equivalent of Ni(II) and 0.7 equivalents of Zn(II). Traces: black, raw data for all samples; dashed green line, best fit model according to Table 1 (fits 1, 3, and 5). All remaining EXAFS data are collected in Table S2, Supporting Information.

data. This may be attributed to the large correlation between the three sulfur donors and the lone N donor, making it difficult to properly resolve the distances of the two shells when the other parameters were fixed. A 5-coordinate model also resulted in a reasonable fit (fit 2, Table S2, Supporting Information), but there is no evidence to support this type of site from the near-edge spectra.

Upon loading Ni(II)-HypB with zinc in the second site (Ni(II)/Zn(II)-HypB, Figure 4E and F), the nickel EXAFS is similar to that of the high-affinity site in the absence of zinc (Figure 4A), but small differences between the two samples are observed in the FT at 1.9 Å (compare Figure 4F and B). The small shoulder at this distance is indicative of (N/O) ligands and is more resolved when compared to the same shoulder in the FT of the Ni(II)-HypB sample. In addition, the transform magnitude of the peak corresponding to Ni(II)-S at 2.2 Å is slightly smaller, although the difference does not correspond to one whole sulfur donor. These changes may reflect a Ni(II) site with a decreased sulfur contribution, as indicated by the near-edge spectra analysis, but a comparison of EXAFS model fits to S_3(N/O) or S_2(N/O)$_2$ coordination spheres (fit 5 and fit 6, respectively, Table 1) did not reveal dramatically different *F*-factor values. On the basis of these fits, it is not possible to conclude that there is a complete donor exchange in the high-affinity Ni(II) site when Zn(II) is bound in the second site; therefore, the best fit shown (Figure 4E and F) represents the S_3(N/O) model. The bond distances calculated for the Ni(II)-S shell is slightly shorter than that for Ni(II)-HypB at 2.15 Å, and the Ni(II)-N shell is slightly longer at 2.02 Å (Table 1, fit 5).

For the Ni(II)-loaded G-domain, the best model arose from fitting the data (Figure 4C and D) to five N/O ligands at

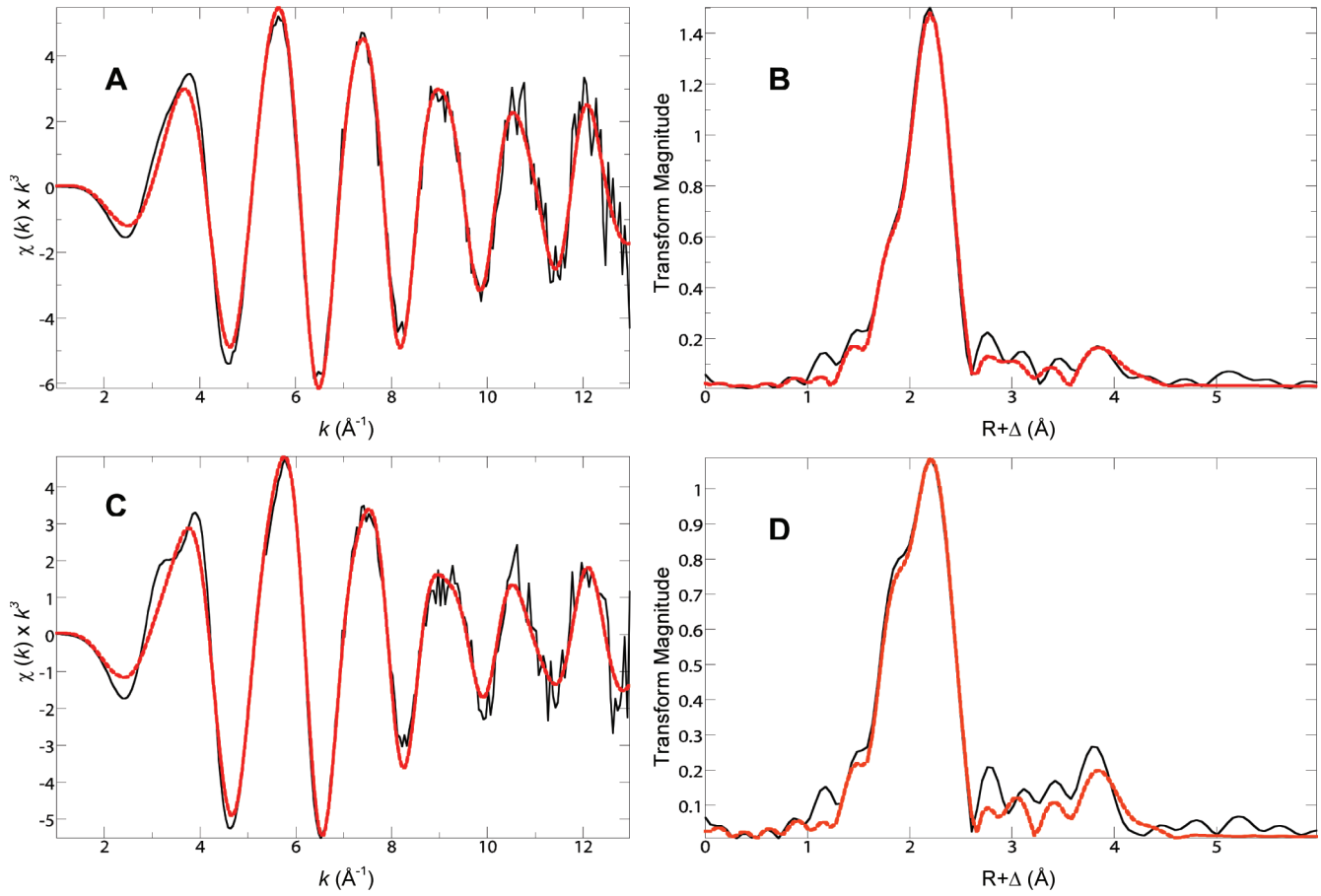

FIGURE 5: k^3-Weighted Zn(II) EXAFS data (left) and Fourier Transform data (right). (A and B) G-domain loaded with 0.5 equivalents of Zn(II). (C and D) HypB loaded with 1 equivalent of Ni(II) and 0.7 equivalents of Zn(II). Traces: black, raw data for all samples; dashed red line, best fit model according to Table 2 (fits 1 and 3). All remaining EXAFS data are collected in Table S3, Supporting Information.

2.07 Å and one sulfur donor at 2.17 Å (Table 1, fit 3) forming an octahedral complex as indicated by the near-edge spectra (Figure 2). The bond distances observed are in agreement with other octahedral Ni(II) complexes (*35, 36*), while a search of the CSDB (Cambridge Structural Database) revealed one complex with a similar coordination sphere (5N/O and 1 S) and bond distances (*37*). An additional model (Table 1, fit 4) with purely N/O-based ligands was also attempted and produced a reasonable fit with only a slightly higher *F* value (0.209 compared to 0.171). When a fit was attempted with more than one sulfur donor, the bond distances were reasonable, but the Debye−Waller factor was extremely high and out of bounds for values observed for Ni−S ligands (fit 3, Table S2, Supporting Information). This result is somewhat surprising given that mutagenesis studies suggest that both C166 and C198 are nickel ligands, although the C198A mutation only weakens nickel binding (*15*). Furthermore, there are clearly two cysteine residues involved when zinc binds to this site (see below). It is possible that the presence of a high number of oxygen or nitrogen donors within this site makes it difficult to resolve the exact number of sulfur donors, a problem if the Ni−S signals in the EXAFS region are 180° out of phase with Ni−N/O interactions. Finally, the mutagenesis experiments also demonstrated the presence of at least one histidine ligand (H167) in the low-affinity site (*15*). In support of this assignment, the intensity of the outer shell peaks in the 3−4 Å range of the FT (Figure 4D) are consistent with a single histidine ligand bound to Ni(II). Because of the smaller amplitude of these peaks, an imidazole was included in the best fit (fit 3, Table 1) using an alternate method (*38*). For this calculation, the Ni-Im(N) pathway is incorporated into the first shell of nitrogens at the best fit distance shown above (2.067 A) with a 15° wag of the imidazole ring and α and β angles of 15° and 0°, respectively (*38*).

The Zn EXAFS and FT of the G-domain loaded with Zn(II) in the low-affinity site are shown in Figure 5A and B. Fit 1, Table S3 (Supporting Information) was used to fit four sulfur donors to Zn(II), and as expected, the residuals were still significant (data not shown). The FT of this sample reveals a major peak around 2.3 Å with a poorly resolved shoulder on the low R side typical of those observed for mixed S/N Zn(II) sites (*32, 33*), which is consistent with the near-edge spectra analysis. The fit was thus improved by including an N-donor and excluding one sulfur ligand, with the fit displaying standard Zn−S distances but somewhat short Zn-(N/O) bonds at 1.98 Å (fit 2, Table S3, Supporting Information). The fit, however, was still considered reasonable because of the corresponding low Debye−Waller factors for nitrogen and oxygen. Decreased Debye−Waller factors are common for short bond distances due to lower vibrational frequencies and are indicative of more rigid or constrained bonds (*39*). Increasing the nitrogen contribution (fit 3, Table S3, Supporting Information) in a $ZnS_2(N/O)_2$ ligand sphere did not improve the fit. In contrast, the fit was improved by including a single histidine as indicated by the lower *F* value,

Table 2: Zn(II) EXAFS Curve-Fitting Results for the Low-Affinity Metal Sites in *E. coli* HypB[a,b] (see Table S3, Supporting Information for Additional Fits)

	A-Bs	N	R (Å)	σ^2 (Å^2)	ΔE_0 (eV)	F-factor
			Zn(II)-G-domain			
fit 1	*Zn−S*	*2.5*	*2.293(3)*	*0.00402(1)*	*−15.297(1)*	*0.19*
	Zn−O	*1*	*2.021(13)*	*0.00412(2)*		
	Zn−Zn	*1*	*4.013(21)*	*0.00586(2)*		
	Zn-Im(N)	*0.5*	*1.984(11)*	*0.00453(1)*		
fit 2	Zn−S	2	2.307(3)	0.00278(1)	−14.091(1)	0.206
	Zn−O	1	2.053(10)	0.00186(1)		
	Zn−Zn	1	3.611(79)	0.01903(1)		
	Zn-Im(N)	1	1.978(13)	0.00693(1)		
			Ni(II)/Zn(II)-HypB			
fit 3	*Zn−S*	*2*	*2.293(3)*	*0.00429(1)*	*−14.587(2)*	*0.221*
	Zn−O	*1*	*2.006(8)*	*0.00242(1)*		
	Zn−Zn	*1*	*3.984(21)*	*0.00838(2)*		
	Zn-Im(N)	*1*	*1.954(12)*	*0.00784(1)*		
fit 4	Zn−S	2.5	2.284(3)	0.00543(1)	−16.69(2)	0.238
	Zn−O	1	1.983(9)	0.002(1)		
	Zn−Zn	1	3.952(20)	0.00756(2)		
	Zn-Im(N)	0.5	1.922(10)	0.00978(1)		
fit 5	Zn−S	2	2.3(5)	0.00481(1)	−12.449(2)	0.237
	Zn−O	1	2.024(33)	0.00731(1)		
	Zn-Im(N)	1	1.996(17)	0.00309(1)		

[a] A-Bs denotes absorber and backscatterer interaction; N denotes coordination number; R is given in Å and represents interatomic distances; σ^2 given in Å^2, are the Debeye−Waller factors (mean-square deviations in interatomic distance); the threshold energy shifts, ΔE_0 are given in eV. The values in parentheses are the estimated standard deviations obtained from the diagonal elements of the covariance matrix. The F-factor or fit-error function is defined as $(\Sigma k^6(\chi(k)_{calcd} - \chi(k)_{exptl})^2/\Sigma k^6\chi(k)_{exptl}^2)^{1/2}$. The summation is over all data points included in the refinement. [b] The best fit models are italicized and overlaid in Figure 5.

but the residuals still indicated a missing component in the 3−4 Å range (data not shown). Typical Zn−Zn distances are 3−4 Å and could also account for the features observed in the FT data (*32*). This possibility is supported by the structure of the *M. jannaschii* HypB homologue (*17*), which revealed a dinuclear Zn(II) cluster at the dimerization interface of two protein monomers. A fit based on the ligand shell resolved in this crystal structure was used (see Figure S4, Supporting Information), with two Zn(II) atoms coordinated by an average of 2.5 sulfurs, 1 water molecule, 0.5 imidazoles, and 1 Zn−Zn interaction, and this fit produced the lowest F factor (fit 1, Table 2 and Figure 5A and B). The Zn−S distances of 2.29 Å, Zn−O distance of 2.02 Å, and histidine donor with a Zn−N_{Im} distance of 1.98 Å are in close agreement with zinc−ligand bond distances previously reported for model complexes or other zinc metalloproteins (*38, 40−42*). When a symmetrical model (see analysis of the full-length protein below) was used (fit 2, Table 2) the fit produced a Zn−Zn distance (3.61 Å) similar to that modeled into the crystal structure from *M. jannaschii* (3.65 Å), but the accompanying Debye−Waller factor was unreasonably high at 0.01903 Å^2. In this light, an unsymmetrical dimeric ligand sphere consisting of only a 0.5 histidine contribution per zinc ion (fit 1, Table 2) was considered the most likely structure for this site.

In order to determine if the low-affinity zinc site has a similar structure in the context of full-length HypB with nickel in the N-terminal site as in the isolated G-domain, the EXAFS and FT for this sample was also analyzed (Figure 5C and D). At first glance, the FT's of the low-affinity site in the full-length protein and the G-domain are somewhat similar; however, a small difference can be observed in the higher intensity of the poorly resolved shoulder of the main 2.3 Å peak. Sulfur (high Z) backscattering dominates Zn(II) EXAFS; therfore, it is probable that a decrease in the sulfur content resulted in a less obscured (N/O) (low-Z) backscattering peak. Furthermore, the transform magnitude of the sulfur peak is lower than that observed for the isolated Zn(II)-G-domain. These data are consistent with our near-edge spectra analysis that indicated lower sulfur content in the full-length protein (*32, 43*). There also appears to be stronger histidine coordination because the first peak in the EXAFS contains a more distinct shoulder or camel hump feature, and the signal contribution at 3−4 Å of the FT is slightly more intense (*44*). Fitting the data to the same coordination sphere as the best fit model for the Zn(II)-G-domain (fit 4, Table 2) was reasonable; however, there were clearly still contributions in the 3−4 Å range that were not accounted for, indicating increased histidine contributions. The best fit for the full-length protein was obtained when the coordination sphere was slightly altered by dropping a sulfur donor and increasing the N value for an imidazole donor by 0.5 (to $N = 1$), creating a symmetrical dinuclear Zn(II) site (fit 3, Table 2). The bond distances calculated were all reasonable, although the Zn−Zn distance of 3.98 Å is slightly longer than those previously observed for zinc dinuclear sites (*32*). A comparison of residuals from fit 3, Table 2 (Figure S2, Supporting Information) with a fit that is the same except that it lacks a Zn−Zn shell (fit 5, Table 2) reveals the contribution of this shell to the data in the 3−4 Å range. This improvement, in combination with a decreased F value, supports the presence of a dinuclear site and represents the most likely Zn(II) coordination environment in the low-affinity site of full-length HypB with Ni(II) present in the high-affinity site.

DISCUSSION

It is clear from previous genetic studies that HypB is necessary for the successful maturation of the *E. coli* [NiFe] hydrogenase enzymes with a role in nickel incorporation (*3, 14, 26, 27*). Along with the essential GTPase activity (*3*), *E. coli* HypB has a high-affinity N-terminal Ni(II) site and a low-affinity metal site localized within the GTPase domain with a preference for Zn(II) over Ni(II) (*15*). The experiments performed in this study demonstrate that both sites contribute to hydrogenase biosynthesis *in vivo* and shed some light on the structures of each site in the purified protein.

EXAFS and near-edge spectra analysis of the high-affinity site of HypB loaded with Ni(II) reveal a S_3(N/O) coordination environment with a square-planar geometry. The modeling of 3 sulfur ligands is consistent with the observation that Ni(II) binding at this site is severely inhibited by substituting alanine residues for C2, C5, and/or C7 (*15*). The assignment of the fourth (N/O) ligand, however, is not as straightforward because there are a large number of potential metal-binding residues distributed throughout the rest of the protein. There are 2 histidines in close proximity to the N-terminus (H19, H22), but a role for histidine in the high-affinity site can be excluded because the FT did not indicate any pronounced

signals at 3−4 Å. This leaves a number of local aspartates (D17) or glutamates (E9, E15, E18) as possible O donors, backbone amides, or the N-terminal amino group as possible N donors, as well as more distant residues as potential ligands.

The hydrogenase deficiency of a Δ*hypB* strain is not complemented by the expression of HypB containing mutations at C2, C5, and C7. Furthermore, the single C7A mutant, which still binds nickel but with a much weaker affinity than wild-type protein (*15*), only restores a low level of activity to the Δ*hypB* strain. These observations suggest that the tightly bound nickel at this N-terminal site is necessary for HypB's role in hydrogenase production. However, the incomplete conservation of the N-terminal cysteine motif in all HypB homologues suggests that this nickel site on *E. coli* HypB meets a specialized requirement of this organism. A square-planar geometry is favorable for Ni(II) complexes (*45*); therefore, this type of coordination explains the preference of the high-affinity site of HypB for nickel over zinc (*15*). Square-planar sites have been observed in several nickel proteins, including the acetyl-CoA synthase and nickel-superoxide dismutase enzymes as well as the amino-terminal copper- and nickel-binding (ATCUN) motif of albumin proteins (*46*−*49*), although none have the S_3(N/O) ligands of HypB. The ATCUN motif is of particular interest because it is a terminal metal transport site (*46*). In analogy with the ATCUN motif, the high-affinity N-terminal site of HypB may function as a source of accessible nickel for the hydrogenase enzymes, perhaps under conditions when nickel ions are scarce. In support of this hypothesis, a recent study demonstrated that the complete high-affinity nickel site of HypB is localized to the immediate N-terminal sequence of the protein (*50*). In the context of the complete nickel insertion complex, the affinity of this site may be weakened such that the nickel can be transferred to a partner protein or the hydrogenase enzyme precursor protein. For example, another accessory protein SlyD forms a complex with HypB and modulates the accessibility of the nickel ion in the high-affinity site (*51*).

Mutation of C166 or H167, two of the ligands in the low-affinity site, eliminates hydrogenase production under standard conditions, and as with the high-affinity site mutants, partial complementation was observed upon expression of the mutants in the presence of excess nickel (1 mM). These observations indicate that the low-affinity site must also be competent at metal binding for proper incorporation of Ni(II) into the hydrogenase active site. The G-domain of HypB can bind an equivalent of either Ni(II) or Zn(II) (*15*), and the fact that zinc can compete with nickel indicates that only one metal ion can fill what must be at least partially overlapping sites, but which metal occupies it *in vivo* is not clear. However, the coordination geometries observed for Ni(II) and Zn(II) differ, suggesting that this low-affinity site of HypB is flexible and could possibly accommodate other divalent metals. A change in coordination environment upon metal substitution at the same location is common among a number of metalloproteins (for example, see refs *38, 52,* and *53*). A dinuclear site is observed in the presence of Zn(II), and in analogy with the *M. jannaschii* homologue, this site probably sits at the interface of a protein dimer. In contrast, there is no significant peak present in the FT of the Ni(II)-loaded G-domain at 3−4 Å to support a Ni−Ni interaction. However, it is likely that the nickel site also bridges a protein dimer because analytical ultracentrifugation experiments reveal that at the concentrations used for the spectroscopic analysis the protein is a dimer in the presence of either nickel or zinc (Figure S3, Supporting Information and unpublished data). It has not been established that HypB functions as a dimer *in vivo*, but given that both monomers in the *M. jannaschii* structure contact the two GTP molecules at the dimeric interface (*17*), it is likely that the GTPase is only active in the context of the dimer.

The EXAFS data for Zn(II) loaded in the low-affinity site of both the full-length protein and the isolated G-domain reveal four-coordinate metals in the dinuclear Zn(II) complex. The best fit of the EXAFS from the G-domain was obtained by using an asymmetric model based on the *M. jannaschii* crystal structure, suggesting that the *E. coli* protein has a very similar site. The asymmetry of the G-domain site is explained by the observation that H96 (H167 in the *E. coli* protein) from only one monomer serves as a ligand, while H96 from the other monomer is sequestered by an aromatic stacking interaction with the invariant F131 (F202, *E. coli*) (*17*). Zn(II) XAS of HypB loaded with Ni(II) in the high-affinity site and Zn(II) in the low-affinity site indicates that in the full-length protein the latter site adopts a slightly different conformation with more symmetry, possibly by recruiting the histidine residue, H167, from the second monomer to replace one of the cysteine ligands.

These data support the hypothesis that the presence of nickel in the N-terminal domain of the protein influences the coordination of the low-affinity site metal, although the possibility that the N-terminal protein sequence alone causes the same effect cannot be ruled out. The change in the Zn(II) coordination sphere of the low-affinity site in the full-length protein compared to the isolated G-domain is relatively small, but it may play a role in the Ni(II) delivery process. The Zn(II)-binding residue, C198, is part of a highly conserved GTPase motif called switch II, which connects GTP hydrolysis to the function of the protein through a conformational change (*54*). This switch region in the *M. jannaschii* HypB structure was postulated to link nucleotide switching, dimer formation, and metal coordination through global structural changes (*17*). Therefore, for *E. coli* HypB it is reasonable to suggest that upon binding nickel in the high-affinity site there is a subtle reorganization of the low-affinity site, such as binding of the second H167 ligand to replace C198, which leads to a conformational change that provides communication between the GTP-binding domain and the two metal sites. A similar communication between two distinct metal sites was also observed in a recent XAS study of *Helicobacter pylori* HypA (*55*).

This hypothesis is further substantiated by the changes in the XAS of the high-affinity Ni(II) site upon loading Zn(II) in the low-affinity site. After Zn(II) was added to the Ni(II)-HypB sample, there was a clear change in the edge structure, and it was no longer possible to differentiate between two different models (S_3(N/O) vs $S_2(N/O)_2$), indicating that the structure of the Ni(II)-loaded high-affinity site is influenced by the Zn(II). The bond lengths calculated for the Ni(II)-S shell were as expected for a square-planar Ni(II) complex; however, the lone Ni(II)-N/O shell was fit to a long bond distance (2.02 Å compared to 1.87 Å in the Ni(II)-HypB sample). It is possible that in the presence of Zn(II) the high-

affinity site or N-terminal domain becomes more flexible and undergoes a small conformational change leading to a slight distortion in the square-planar coordination. The decrease in sulfur contribution may be the result of partial exchange of a sulfur donor for a water molecule or backbone amides. Mutants lacking any one of the cysteines in the CXXCGC motif can still bind nickel *in vitro*, although with much weaker affinity, demonstrating that one thiolate can be replaced by a different ligand (*15*).

The function of the low-affinity metal site in the G-domain of HypB is not clear, but a number of GTPases contain structural Zn(II) sites (*56*−*59*). For example, a similar dinuclear Zn(II) site in UreG, the GTPase involved in urease production (*2*), is in close proximity to an intrinsically unstructured region, as observed by solution NMR studies (*56*). Zambelli and co-workers suggested that Zn(II) binding could induce a conformational change and contribute to the stabilization of these unstructured regions (*56*). In analogy, metal binding to the G-domain of HypB could have structural consequences that influence the N-terminal Ni(II) site as well as the GTPase activity, which may drive Ni(II) delivery to the hydrogenase. Another possible model is that the second metal site in HypB is the source of nickel for the hydrogenase and/or is involved in sensing that the nickel is properly inserted into the hydrogenase active site and then activating GTPase hydrolysis (*15*), thus advancing the pathway forward to the next step in enzyme production. A careful analysis of the connection between the rates of GTP hydrolysis and metal binding to the individual sites on HypB is the next step in the elucidation of HypB's function.

The essential nature of both of the metal sites of HypB and the GTPase activity, combined with the structural information, suggests that HypB participates in two integral aspects of the nickel insertion step of hydrogenase biosynthesis: nickel delivery and signaling. HypB does not function on its own; therefore, it is very likely that the additional accessory proteins required for nickel insertion, such as HypA and SlyD, will affect the properties of HypB (*51*). The detailed characterization of the metal-binding sites of HypB reported here will serve as a baseline for future spectroscopic analysis in the context of additional accessory proteins and the complete nickel insertion complex, providing more information on the mechanism of nickel insertion during hydrogenase metallocenter assembly.

ACKNOWLEDGMENT

We thank Dr. G. Butland and Professor A. Emili (Banting and Best Institute, University of Toronto) for the Δ*hypB* strain of *E. coli*, Professor A. Böck for the HypB antibody, and Harini Kaluarachchi for assistance in the running of additional XAS samples. Portions of this research were carried out at the Stanford Synchrotron Radiation Laboratory, a national user facility operated by Stanford University on behalf of the U.S. Department of Energy, Office of Basic Energy Sciences. The SSRL Structural Molecular Biology Program is supported by the Department of Energy, Office of Biological and Environmental Research, and by the National Institutes of Health, National Center for Research Resources, Biomedical Technology Program.

SUPPORTING INFORMATION AVAILABLE

Tables S1−S3 containing PCR primer sequences and additional EXAFS curve fitting analysis; Figures S1−S4 show a near-edge comparison of Ni(II)-HypB to model complexes, a residual comparison corresponding to fit 3 and fit 5 of Table 2, Zn(II)-G-domain analytical ultracentrifugation data, and a schematic representation of the low-affinity Zn(II) cluster from *Methanocaldococcus jannaschii* HypB, respectively. This material is available free of charge via the Internet at http://pubs.acs.org.

REFERENCES

1. Mulrooney, S. B., and Hausinger, R. P. (2003) Nickel uptake and utilization by microorganisms. *FEMS Microbiol. Rev. 27*, 239–261.
2. Kuchar, J., and Hausinger, R. P. (2004) Biosynthesis of metal sites. *Chem. Rev. 104*, 509–526.
3. Maier, T., Lottspeich, F., and Böck, A. (1995) GTP hydrolysis by HypB is essential for nickel insertion into hydrogenases of *Escherichia coli*. *Eur. J. Biochem. 230*, 133–138.
4. Soriano, A., and Hausinger, R. P. (1999) GTP-dependent activation of urease apoprotein in complex with the UreD, UreF, and UreG accessory proteins. *Proc. Natl. Acad. Sci. U.S.A. 96*, 11140–11144.
5. Jeon, W. B., Cheng, J., and Ludden, P. W. (2001) Purification and characterization of membrane-associated CooC protein and its functional role in the insertion of nickel into carbon monoxide dehydrogenase from *Rhodospirillum rubrum*. *J. Biol. Chem. 276*, 38602–38609.
6. Loke, H. J., and Lindahl, P. A. (2003) Identification and preliminary characterization of AcsF, a putative Ni-insertase used in the biosynthesis of acetyl-CoA synthase from *Clostridium thermoaceticum*. *J. Inorg. Biochem. 93*, 33–40.
7. Mehta, N., Benoit, S., and Maier, R. J. (2003) Roles of conserved nucleotide-binding domains in accessory proteins, HypB and UreG, in the maturation of nickel-enzymes required for efficient *Helicobacter pylori* colonization. *Microb. Pathogen. 35*, 229–334.
8. Böck, A., King, P. W., Blokesch, M., and Posewitz, M. C. (2006) Maturation of hydrogenases. *Adv. Micro. Physiol. 51*, 1–71.
9. Forzi, L., and Sawers, G. (2007) Maturation of [NiFe]-hydrogenases in *Escherichia coli*. *BioMetals 20*, 565–578.
10. Leach, M. R., and Zamble, D. B. (2007) Metallocenter assembly of the hydrogenase enzymes. *Curr. Opin. Chem. Biol. 11*, 159–165.
11. Zhang, J. W., Butland, G., Greenblatt, J. F., Emili, A., and Zamble, D. B. (2005) A role for SlyD in the *Escherichia coli* hydrogenase biosynthetic pathway. *J. Biol. Chem. 280*, 4360–4366.
12. Cammack, R. (2001) Hydrogenase in Biotechnology, in *Hydrogen As a Fuel: Learning from Nature* (Cammack, R., Frey, M., and Robson, R., Eds.) pp 181−200, Taylor & Francis, New York.
13. Rao, K. K., and Cammack, R. (2001) Producing Hydrogen As a Fuel, in *Hydrogen As a Fuel: Learning from Nature* (Cammack, R., Frey, M., and Robson, R., Eds.) pp 201−230, Taylor & Francis, New York.
14. Maier, T., Jacobi, A., Sauter, M., and Böck, A. (1993) The product of the *hypB* gene, which is required for nickel incorporation into hydrogenases, is a novel guanine nucleotide-binding protein. *J. Bacteriol. 175*, 630–635.
15. Leach, M. R., Sandal, S., Sun, H., and Zamble, D. B. (2005) The metal-binding activity of the *Escherichia coli* hydrogenase maturation factor HypB. *Biochemistry 44*, 12229–12238.
16. Robson, R. (2001) The Assembly Line, in *Hydrogen As a Fuel: Learning from Nature* (Cammack, R., Frey, M., and Robson, R., Eds.) pp 57−72, Taylor & Francis, New York.
17. Gasper, R., Scrima, A., and Wittinghofer, A. (2006) Structural insights into HypB, a GTP-binding protein that regulates metal binding. *J. Biol. Chem. 281*, 27492–27502.
18. Yu, D., Ellis, H. M., Lee, E.-C., Jenkins, N. A., Copeland, N. G., and Court, D. L. (2003) An efficient recombination system for chromosome engineering in *Escherichia coli*. *Proc. Natl. Acad. Sci. U.S.A. 97*, 5978–5983.
19. Ballantine, S. P., and Boxer, D. H. (1985) Nickel-containing hydrogenase isoenzymes from anaerobically grown *Escherichia coli* K-12. *J. Bacteriol. 163*, 454–459.

20. Atanassova, A., Lam, R., and Zamble, D. B. (2004) A high-performance liquid chromatography method for determining transition metal content of proteins. *Anal. Biochem. 335*, 103–111.
21. Cramer, S. P., Tench, O., Yocum, M., and George, G. N. (1988) A 13-element Ge detector for fluorescence EXAFS. *Nucl. Instrum. Methods Phys. Res., Sect. A 266*, 586–591.
22. George, G. N., Garrett, R. M., Prince, R. C., and Rajagopalan, K. V. (1996) The molybdenum site of sulfite oxidase: a comparison of wild-type and the cystein 207 to serine mutant using X-ray absorption spectroscopy. *J. Am. Chem. Soc. 118*, 8588–8592.
23. Rehr, J. J., Mustre de Leon, J., Zabinsky, S. I., and Albers, R. C. (1991) Theoretical X-ray absorption fine structure standards. *J. Am. Chem. Soc. 113*, 5135–5140.
24. Guzman, L.-M., Belin, D., Carson, M. J., and Beckwith, J. (1995) Tight regulation, modulation, and high-level expression by vectors containing the arabinose PBAD promoter. *J. Bacteriol. 177*, 4121–4130.
25. Hube, M., Blokesch, M., and Böck, A. (2002) Network of hydrogenase maturation in *Escherichia coli*: role of accessory proteins HypA and HypF. *J. Bacteriol. 184*, 3879–3885.
26. Lutz, S., Jacobi, A., Schlensog, V., Böhm, R., Sawers, G., and Böck, A. (1991) Molecular characterization of an operon (*hyp*) necessary for the activity of the three hydrogenase isoenzymes in *Escherichia coli*. *Mol. Microbiol. 5*, 123–135.
27. Waugh, R., and Boxer, D. H. (1986) Pleiotropic hydrogenase mutants of *Escherichia coli* K12: growth in the presence of nickel can restore hydrogenase activity. *Biochimie 68*, 157–166.
28. Colpas, G. J., Maroney, M. J., Bagyinka, C., Kumar, M., Willis, W. S., Suib, S. L., Baidya, N., and Mascharak, P. K. (1991) X-ray spectroscopic studies of nickel complexes, with application to the structure of nickel sites in hydrogenases. *Inorg. Chem. 30*, 920–928.
29. Maroney, M. J., Colpas, G. J., Bagyinka, C., Baidya, N., and Mascharak, P. K. (1991) EXAFS investigations of the Ni site in *Thiocapsa roseopersicina* hydrogenase: evidence for a novel Ni, Fe, S cluster. *J. Am. Chem. Soc. 113*, 3962–3972.
30. Musgrave, K. B., Laplaza, C. E., Holm, R. H., Hedman, B., and Hodgson, K. O. (2002) Structural characterization of metallopeptides designed as scaffolds for the stabilization of nickel(II)-Fe(4)S(4) bridged assemblies by X-ray absorption spectroscopy. *J. Am. Chem. Soc. 124*, 3083–3092.
31. Al-Mjeni, F., Ju, T., Pochapsky, T. C., and Maroney, M. J. (2002) XAS investigation of the structure and function of Ni in acireductone dioxygenase. *Biochemistry 41*, 6761–6769.
32. Penner-Hahn, J. E. (2005) Characterization of "spectroscopically quiet" metals in biology. *Coord. Chem. Rev. 249*, 161–177.
33. Clark-Baldwin, K., Tierney, D. L., Govindaswamy, N., Gruff, E. S., Kim, C., Berg, J., Koch, A., and Penner-Hahn, J. E. (1998) The limitations of X-ray absorption spectroscopy for determining the structure of zinc sites in proteins. When is a tetrathiolate not a tetrathiolate? *J. Am. Chem. Soc. 120*, 8401–8409.
34. Krüger, H.-K., Peng, G., and Holm, R. H. (1991) Low-potential nickel(III,II) complexes: new systems based on tetradentate amidate-thiolate ligands and the influence of ligand structure on potentials in relation to the nickel site in [NiFe]-hydrogenases. *Inorg. Chem. 30*, 734–742.
35. Davidson, G., Clugston, S. L., Honek, J. F., and Maroney, M. J. (2001) An XAS investigation of product and inhibitor complexes of Ni-containing GlxI from *Escherichia coli*: mechanistic implications. *Biochemistry 40*, 4569–4582.
36. Lloret, F., Sletten, R., Ruiz, R., Julve, M., Faus, J., and Verdaguer, M. (1992) Oxamidato complexes. 2. Copper(II) and nickel(II) complexes with oxamide-N,N′-diacetic acid: solution study, synthesis, crystal structures, and magnetic properties. *Inorg. Chem. 31*, 778–784.
37. Saalfrank, R. W., Reimann, U., Hampel, F., Goebel, C., and Herbst-Irmer, R. (2003) Metal directed one-pot synthesis: mono-, di- and tetra-nuclear clusters. *Z. Naturforsch., B: Chem. Sci. 58b*, 22–26.
38. Ferreira, G. C., Franco, R., Mangravita, A., and George, G. N. (2002) Unraveling the substrate-metal binding site of ferrochelatase: an X-ray absorption spectroscopic study. *Biochemistry 41*, 4809–4818.
39. Garcia, A. E., Krumhansl, J. A., and Frauenfelder, H. (1997) Variations on a theme by Debye and Waller: from simple crystals to proteins. *Proteins 29*, 153–160.
40. Dauter, Z., Wilson, K. S., Sieker, L. C., Moulis, J. M., and Meyer, J. (1996) Zinc- and iron-rubredoxins from *Clostridium pasteurianum* at atomic resolution: a high-precision model of a ZnS4 coordination unit in a protein. *Proc. Natl. Acad. Sci. U.S.A. 93*, 8836–8840.
41. Jacquamet, L., Aberdam, D., Adrait, A., Hazemann, J.-L., Latour, J.-M., and Michaud-Soret, I. (1998) X-ray absorption spectroscopy of a new zinc site in the fur protein from *Escherichia coli*. *Biochemistry 37*, 2564–2571.
42. McClure, C. P., Rusche, K. M., Peariso, K., Jackman, J. E., Fierke, C. A., and Penner-Hahn, J. E. (2003) EXAFS studies of the zinc sites of UDP-(3-O-acyl)-N-acetylglucosamine deacetylase (LpxC). *J. Inorg. Biochem. 94*, 78–85.
43. VanZile, M. L., Cosper, N. J., Scott, R. A., and Giedroc, D. P. (2000) The zinc metalloregulatory protein *Synechococcus* PCC7942 SmtB binds a single zinc ion per monomer with high affinity in a tetrahedral coordination geometry. *Biochemistry 39*, 11818–11829.
44. Diakun, G. P., Fairall, L., and Klug, A. (1986) EXAFS study of the zinc-binding sites in the protein transcription factor IIIA. *Nature 324*, 698–699.
45. Cotton, F. A., and Wilkinson, G. (1988) *Advanced Inorganic Chemistry*, 5th ed., Wiley-Interscience, New York.
46. Harford, C., and Sarkar, B. (1997) Amino terminal Cu(II)- and Ni(II)-binding (ATCUN) motif of proteins and peptides: metal binding, DNA cleavage, and other properties. *Acc. Chem. Res. 30*, 123–130.
47. Drennan, C. L., Doukov, T. I., and Ragsdale, S. W. (2004) The metalloclusters of carbon monoxide dehydrogenase/acetyl-CoA synthase: a story in pictures. *J. Biol. Inorg. Chem. 9*, 511–515.
48. Barondeau, D. P., Kassman, C. J., Bruns, C. K., Tainer, J. A., and Getzoff, E. D. (2004) Nickel superoxide dismutase structure and mechanism. *Biochemistry 43*, 8038–8047.
49. Wuerges, J., Lee, J.-W., Yim, Y.-I., Yim, H.-S., Kang, S. O., Carugo, K. D., and Fridovich, I. (2004) Crystal structure of nickel-containing superoxide dismutase reveals another type of active site. *Proc. Natl. Acad. Sci. U.S.A. 101*, 8569–8574.
50. Chan Chung, K. C., Cao, L., Dias, A. V., Pickering, I. J., George, G. N., and Zamble, D. B. (2008) A high-affinity metal-binding peptide from *Escherichia coli* HypB, *J. Am. Chem. Soc.* [Online early access]. DOI:10.1021/ja8055003. Published Online: Oct 4, 2008.
51. Leach, M. R., Zhang, J. W., and Zamble, D. B. (2007) The role of complex formation between the *Escherichia coli* hydrogenase accessory factors HypB and SlyD. *J. Biol. Chem. 282*, 16177–16186.
52. Leitch, S., Bradley, M. J., Rowe, J. L., Chivers, P. T., and Maroney, M. J. (2007) Nickel-specific response in the transcriptional regulator *Escherichia coli* NikR. *J. Am. Chem. Soc. 129*, 5085–5095.
53. Phillips, C. M., Shreiter, E. R., Guo, Y., Wang, S. C., Zamble, D. B., and Drennan, C. L. (2008) Structural basis of the metal specificity for nickel regulatory protein NikR. *Biochemistry 47*, 1938–1946.
54. Sprang, S. R. (1997) G protein mechanisms: insights from structural analysis. *Annu. Rev. Biochem. 66*, 639–678.
55. Kennedy, D. C., Herbst, R. W., Iwig, J. S., Chivers, P. T., and Maroney, M. J. (2007) A dynamic Zn site in *Helicobacter pylori* HypA: a potential mechanism for metal-specific protein activity. *J. Am. Chem. Soc. 129*, 16–17.
56. Zambelli, B., Stola, M., Musiani, F., De Vriendt, K., Samyn, B., Devreese, B., Van Beeumen, J., Turano, P., Dikiy, A., Bryant, D. A., and Ciurli, S. (2005) UreG, a chaperone in the urease assembly process, is an intrinsically unstructured GTPase that specifically binds Zn2+. *J. Biol. Chem. 280*, 4684–4695.
57. Fukuda, M. (2002) Synaptotagmin-like protein (Slp) homology domain 1 of Slac2-a/melanophilin is a critical determinant of GTP-dependent specific binding to Rab27A. *J. Biol. Chem. 277*, 40118–40124.
58. Levdikov, V. M., Blagova, E. V., Brannigan, J. A., Cladiere, L., Antson, A. A., Isupov, M. N., Seror, S. J., and Wilkinson, A. J. (2004) The crystal structure of YloQ, a circularly permuted GTPase essential for *Bacillus subtilis* viability. *J. Mol. Biol. 340*, 767–782.
59. Merithew, E., Stone, C., Eathiraj, S., and Lambright, D. G. (2003) Determinants of Rab5 interaction with the N terminus of early endosome antigen 1. *J. Biol. Chem. 278*, 8494–8500.

BI801337X